Synergistic integration of Bi metal and phosphate defects on hexagonal and monoclinic BiPO$_4$: Enhanced photocatalysis and reaction mechanism

Jiarui Li[a], Wendong Zhang[b], Maoxi Ran[a], Yanjuan Sun[a,*], Hongwei Huang[c], Fan Dong[a,d,*]

[a] Chongqing Key Laboratory of Catalysis and New Environmental Materials, College of Environment and Resources, Chongqing Technology and Business University, Chongqing, 400067, China
[b] Chongqing Key Laboratory of Inorganic Functional Materials, Department of Scientific Research Management, Chongqing Normal University, Chongqing, 401331, China
[c] Beijing Key Laboratory of Materials Utilization of Nonmetallic Minerals and Solid Wastes, National Laboratory of Mineral Materials, School of Materials Science and Technology, China University of Geosciences, Beijing 100083, China
[d] Institute of Fundamental and Frontier Sciences, University of Electronic Science and Technology of China, Chengdu 611731, China

ARTICLE INFO

ABSTRACT

Bi metal deposited hexagonal BiPO$_4$ with the exposure of {102} facet (Bi-HBPO-102) and Bi metal deposited monoclinic BiPO$_4$ with the exposure of {120} facet (Bi-MBPO-120) were prepared by chemical deposition method and solvothermal approach, respectively. The as-prepared catalysts presented more efficient photocatalytic activity of NO$_x$ removal than pure BiPO$_4$ (2.0% for BiPO$_4$, 51.4% for Bi-HBPO-102 and 36.2% for Bi-MBPO-120) under visible light irradiation, which can be attributed to the synergistic effects endowed by the phosphate defect, the surface plasmon resonance (SPR) effect of Bi metal and the facet effect. The existence of phosphate defect was confirmed by the XPS and solid state EPR technique. The DFT calculation revealed the position of phosphate and the phosphate defect induced the formation of an intermediate level within the forbidden band to allow efficient charge transfer from valence band to conduction band. Moreover, the Bi metal would act as the electron contributor and electron conductor which facilitated the charge carriers separation. Therefore, a new charge transfer pathway can be certified on account of the fact that the covalent loop was evidently generated both at the interface and along with the path of $[Bi_2O_2]^{2+} \rightarrow$ Bi metal $\rightarrow PO_4^{3-}$ on the Bi@BiPO$_4$. More importantly, the Bi-HBPO-102 with exposure of {102} facet exhibited higher photocatalytic activity than the Bi-MBPO-120 with exposed {120} facet. The {102} facet with the stronger distorted PO$_4$ tetrahedron and the lower potential energy barrier (-17.5eV) contributed to the contacted interface with the more efficient charge transfer, which promoted the generation of active radicals on {102} facet. Additionally, for Bi-HBPO-102, the reaction intermediate NO$^+$ can be observed with in situ DRIFTS, which facilitated the activation of NO via the formation of NO$^+$ to promote the oxidation of NO into final products. Herein, a new strategy for tailoring the charge transfer pathway was developed to enhance the photocatalytic performance and a new photocatalytic reaction mechanism for photocatalytic NO$_x$ removal was proposed. This work could provide new insights into the modification of photocatalysts and mechanistic understanding of the gas-phase photocatalytic reaction mechanism.

1. Introduction

As one kind of typical air pollutants, nitric oxide (NO$_x$), can be generated from the combustion of fossil fuels and the emission of vehicle exhaust, which are the main contributors to photochemical smog and acid rain [1–3]. In recent years, photocatalysis is widely applied to remove the NO$_x$ in the atmospheric environment with little secondary pollution under mild conditions [4–7]. Among various semiconductor photocatalysts, the Bi-based photocatalysts have received broad investigation own to its unique electronic structure and excellent photocatalytic performance, such as BiOX(X = Cl, I, Br) [8,9], (BiO)$_2$CO$_3$ [10], Bi$_2$O$_2$SiO$_3$ [11], Bi$_2$O$_3$ [12–15], BiVO$_4$ [15,16], Bi$_2$WO$_6$ [17–19] and BiPO$_4$ [20,21].

Notability, BiPO$_4$ as an oxyacid salt photocatalyst exhibited outperformed photocatalytic activity towards NO purification due to its special structure of nonmetallic oxygen, which could promote the

separation of the photo-generated charge [22]. Hexagonal BiPO$_4$ and monoclinic BiPO$_4$ exhibit different photocatalytic activity because of the distorted PO$_4$ tetrahedron and the distinct dipole moment [22,23]. In addition, exposure with specific facets could influence on the light absorption and charge transfer via the surface atomic arrangements, which would further impact the photocatalytic activity and selectivity [24–26]. Thus, it is feasible to improve the photocatalysts efficiency by constructing the different phase with selective exposed facets.

However, the separation efficiency of photo-induced electron-hole pairs of BiPO$_4$ and utilization of visible light were largely hampered by the wide band gap (4.1 eV) [22]. Interestingly, Bi metal demonstrated a surface plasmon effect (SPR) similar to that of the noble metals and could be functioned as electron contributor and electron conductor, which is beneficial for the charge carriers separation [27]. In addition, the effects of the vacancies are regarded to be a vital factor to tune the optical and catalysts property [28–30]. More importantly, with the optimization of interfacial property via the phosphate defect could offer a new strategy to promote the optical and photocatalytic efficiency of BiPO$_4$.

Herein, Bi metal deposited hexagonal@defective BiPO$_4$ with the exposed {102} facet (Bi-HBPO-102) and Bi metal deposited monoclinic@defective BiPO$_4$ with the exposed {120} facet (Bi-MBPO-120) were prepared by the chemical deposition method and a one-step solvothermal approach, respectively. Due to the synergistic effects of the Bi metal and phosphate defect, the photocatalytic NO removal ratio of modified BiPO$_4$ was highly improved compared to the pure BiPO$_4$ (2.0% for BiPO4 alone while 51.4% for Bi-HBPO-102 and 36.2% for Bi-MBPO-120). Meanwhile, the new charge transfer pathways have been presented based on the fact that the covalent loop are generated at the interface along the path of [Bi$_2$O$_2$]$^{2+}$ → Bi metal → PO$_4$$^{3-}$ on the modified BiPO$_4$. The photocatalytic NO oxidation mechanism was further revealed by the in situ DRIFT. In summary, this work provided the new perspectives on the charge transfer pathway and photocatalysis mechanism for enhancing the photocatalytic performance by optimizing interfacial surface properties.

2. Experimental section

2.1. Materials and synthesis

2.1.1. Synthesis of BiPO$_4$

All the reagents employed in this study were analytical grade and used without further purification. In a typical synthesis, 1.25 mmol of Bi(NO$_3$)$_3$·5H$_2$O and 2.5 mmol of Na$_3$PO$_4$ were added to 46 mL of distilled water at room temperature. Afterwards, HNO$_3$ (4 mol/L, 1 mL) solution was also added into the above-mentioned mixture and stirred for 30 min. The monoclinic phase BiPO$_4$ was hydrothermal treatment of the precursor solution at 180 °C for 24 h. The hexagonal phase BiPO$_4$ was prepared by aging the precursor solution for 30 min at room temperature. Both the two samples were rinsed four times with water and ethanol and dried at 60 °C for 12 h, which were denoted as the precursor of the monoclinic BiPO$_4$ (MBPO) and hexagonal BiPO$_4$ (HBPO) for further use.

2.1.2. Synthesis of Bi-deposited defective BiPO$_4$

In a typical experiment, 0.5 g of MBPO (HBPO) and 0.5 g PVP (polyvinyl pyrrolidone) were added into 50 mL of deionized water with magnetically stirred for 20 min. Next, the concentration of NaBH$_4$ (50 mmol/L, 30 mL) was added drop wise into this suspension, and then stirred for 30 min and aged for another 30 min. The obtained solution were washed with water and ethanol four times, afterwards dried at 40 °C to get the solid products, which were labeled as Bi-MBPO-120 and Bi-HBPO-102, respectively.

2.2. Characterization

X-ray diffraction was performed to analyze the crystal phases of the sample using Cu Kα radiation (XRD: model D/max RA, Rigaku Co. Japan). X-ray photoelectron spectroscopy (XPS) with AlKa X-ray radiation (hm = 1486.6 eV) operated at 150 W (Thermo ESCALAB 250, USA) was used to investigate the surface properties. To characterize the morphology of the samples, SEM images (SEM, JEOL model JSM-6490, Japan) were used. TEM images were used to reveal the morphology and structure of the obtained samples (TEM: JEM-2010, Japan). UV–vis diffuse-reflectance spectrometry (DRS) was performed for the dry-pressed disk samples using a Scan UV–vis spectrophotometer (TU-1901, China) equipped with an integrating sphere assembly, using 100% BaSO4 as the reflectance sample. Photoluminescence (PL) studies (F-7000, HITACHI, Japan) were conducted to investigate the optical properties of the samples. Steady and time-resolved fluorescence emission spectra were recorded at room temperature with a fluorescence spectrophotometer (Edinburgh Instruments, FLSP-920). Samples for ESR measurement were prepared by mixing the samples in 50 mM DMPO solution tanks (aqueous dispersion for DMPO ·'OH and methanol dispersion for DMPO· ˙O$_2^-$) and irradiated with visible light. Electron paramagnetic resonance (EPR) measurements were carried out on a Bruker ESP 500 spectrometer.

2.3. Visible light photocatalytic activity

The photocatalytic activity was investigated by determining the removal ratio of NO at ppb level (500 ppb) in a continuous-flow reactor (rectangular reactor, 30 × 15 × 10 cm), made of polymeric glass covered with Saint-Glass. A 150 W commercial tungsten halogen lamp was vertically placed outside the reactor. A UV cutoff filter (420 nm) was utilized to remove the UV light in the light beam. The as-prepared sample (0.20 g) was dispersed and coated onto two glass dishes (12.0 cm in diameter) for photocatalytic activity tests. After the adsorption-desorption equilibrium was achieved, the lamp was turned on. The concentration of NO was continuously measured by a NO$_x$ analyser (Thermo Environmental Instruments Inc., model 42c-TL). The removal ratio (η) of NO was calculated as η (%) = (1 − C/C$_0$) × 100%, where C and C$_0$ are concentrations of NO in the outlet steam and the feeding stream, respectively.

2.4. DFT calculations

Spin-polarized DFT-D2 calculations were conducted using the "Vienna ab initio simulation package" (VASP5.4) [31,32], applying a generalized gradient correlation functional [33]. A plane-wave basis set with cut-off energy 400 eV within the framework of the projector-augmented wave method was employed [34,35]. The Gaussian smearing width was set to 0.2 eV. The Brillouin zone was sampled with a 3 × 3 × 2 Monkhorst Pack grid. All atoms were converged to 0.01 eV Å^{-1}. Hybrid functional based on the Heyd-Scuseria-Ernzerhof (HSE06) method [36,37] were applied to estimate the exact band structures [38].

2.5. In situ DRIFTS study on photocatalytic oxidation of NO process

In situ DRIFTS measurements were conducted using a Tensor II FT-IR spectrometer (Bruker) equipped with an in situ diffuse reflectance cell (Harrick).The photocatalysts were put into the cell. Firstly, He gas (100 mL min^{-1}) was used to remove the residual hydrocarbons, H$_2$O and CO$_2$. The real-time FTIR spectrum after ventilation was utilized as the background. Then, the reaction mixtures (50 mL min^{-1} of NO, 50 mL min^{-1} of O$_2$) were introduced into the cell. NO adsorption on the catalysts was carried out for 20 min. Next, the photocatalysts were illuminated by a visible light source (MUA-210) for 1 h. Realtime FTIR spectra were obtained every two minutes. Meanwhile, the gas fluxes
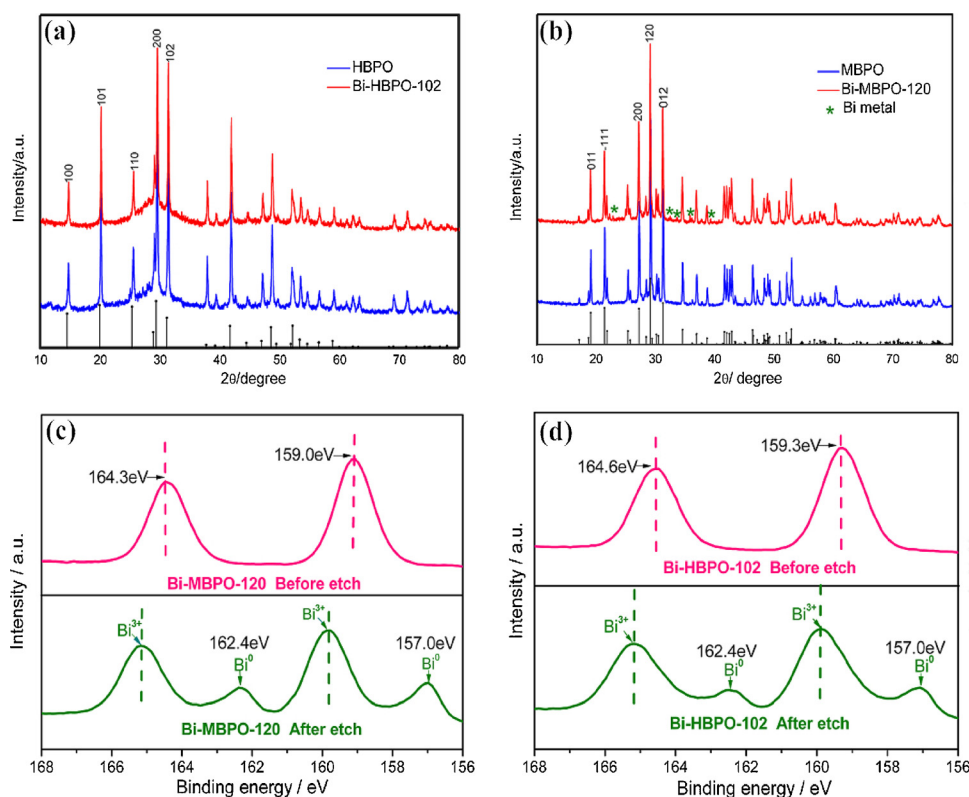
Fig. 1. XRD spectra of HBPO, Bi-HBPO-102(a) and MBPO, Bi-MBPO-120(b); the XPS spectra of Bi-MBPO-120 and Bi-HBPO-102 before and after surface etching; the XPS spectra for Bi 4f (c, d).

were kept the same (50 mL min^{-1} of NO, 50 mL min^{-1} of O$_2$). Finally, FTIR spectra were obtained every two minutes with the same gas fluxes after turning off the light. The IR scanning range between 4000 and 600 cm^{-1} was analyzed to reveal the photocatalytic oxidation process on the catalysts.

3. Results and discussion

3.1. Structural and chemical composition

Fig. 1 reflects the XRD patterns of the as-prepared BiPO$_4$ samples. The main diffraction peaks of HBPO (Fig. 1a) can be nicely indexed to a hexagonal phase (JCPDS Card No.45–1370) and no other impurities can be detected. As shown in Fig. 1b, the typical peaks of MBPO samples can be attributed to monoclinic BiPO$_4$ phase (JCPDS Card No.80-0209). Moreover, the peaks of Bi metal (JCPDS card No 05-0519) are observed in Fig. 1b. However, no characteristic peaks of Bi can be detected in Fig. 1a, which probably indicated its low content and high dispersion of Bi metal. Notably, the {102} peak in (Fig. 1a) are much stronger than the {100}, {101} and {110} peaks in contrast with the standard card of hexagonal phase. A similar situation can be observed in Fig. 1b. In comparison with standard card of monoclinic BiPO$_4$ phase, the other peaks are evidently weaker than the {120} peak. These results imply that the Bi-HBPO-102 and Bi-MBPO-120 samples have the exposure of {102} and {120} facets, respectively. Further detailed information of the exposure of faces will be confirmed by the HRTEM images, as will be discussed later.

The detailed chemical composition of the as-prepared samples was investigated by the XPS spectra before and after the etching of photocatalysts. As shown in Fig. 1c, the two bonds of Bi^{+3} appear at 159.0 and 164.3 eV, which indicates the existence of Bi 4f$_{7/2}$ and Bi f$_{5/2}$ for Bi-MBPO-120 before etching, respectively. In Fig. 1d, two strong peaks at 159.3 and 164.6 eV can be indexed to Bi 4f$_{7/2}$ and Bi f$_{5/2}$ with the Bi-HBPO-102 before etching, originating from Bi^{3+}. After etching

treatment, the peaks for the sample of Bi-MBPO-120 (Fig. 1c) and Bi-HBPO-102 (Fig. 1d) both exhibit a shift of 0.6 eV toward higher binding energies, respectively, which probably steam from the interaction between the metallic Bi and BiPO$_4$. The additional peaks of Bi° can be found at 157.0 eV and 162.4 eV in Fig. 1c and d [39], indicating that the Bi metal has been deposited on the surface of BiPO$_4$.

Furthermore, the dominant O 1s located at 531.0 eV can be assigned to the Bi-O bond in Fig. S1a and Fig. S1b before etching [40]. The Bi-MBPO-120 and Bi-HBPO-102 with the binding energy at 133.5 and 132.6 eV are associated with peaks for P 2p, respectively (Fig. S1c and S1d). After the surface etching for 20 nm, the O 1s and P 2p bonds both have a positive chemical shift to higher binding energy in comparison with the sample without etching treatment. These results indicate that the elements would lose more electrons than that of the perfect BiPO$_4$ without metal Bi. The survey spectra show that the Bi, P, O and C elements coexist in the MBPO and HBPO samples, where the C comes from the adventitious carbon from the XPS instrument in Fig. S1e and Fig. S1f.

3.2. Phosphate defect and band structure

After the etching depth for 20 nm, it is worth to note from the Fig. 2a and b that the peak intensities of P 2p and O 1 s are increased along with the increased surface etching time. The results suggest that the PO$_4^{3-}$ anion group on the surface is less than that in the bulk, which indicates the existence of phosphate defects on the surface of Bi-HBPO-102 and Bi-MBPO-120. Moreover, the solid state EPR spectra record the enhanced defect signal phosphate radical that located at 300.5 MT in Fig. 2c and d under low temperature. With the visible light irradiation, the amplified signals can be observed for both Bi-HBPO-102 and Bi-MBPO-120 in Fig. 2c and d, which suggest that the phosphate defects are responsive to visible light, making the carriers transfer in extended region. The density of states (DOS) of the perfect BiPO$_4$ and defective BiPO$_4$ are calculated (Fig. 2e and f). Obviously, the phosphate defect
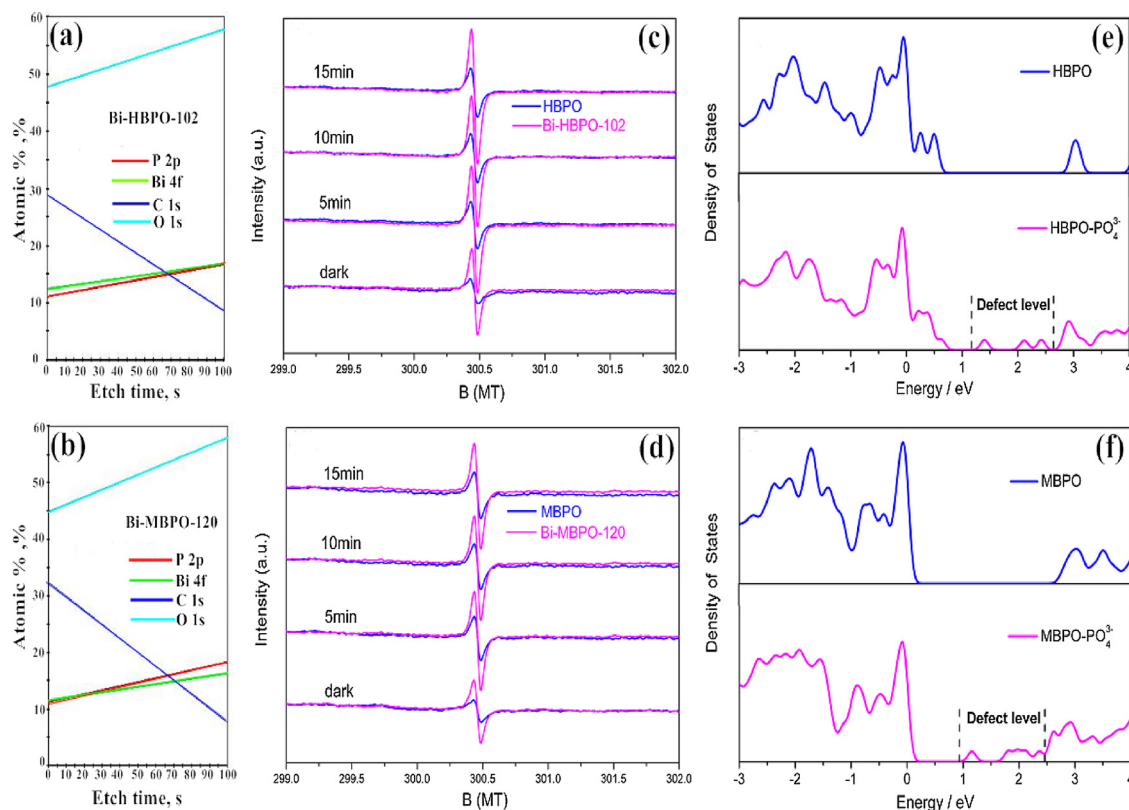
Fig. 2. The element content survey of 100's etching for Bi-HBPO-102 (a) and Bi-MBPO-120 (b); the solid state EPR spectra for HBPO, Bi-HBPO-102, MBPO and Bi-MBPO-120 in dark and with visible-light under low temperature (c and d); the density of states of HBPO and defective hexagonal $BiPO_4$ (HBPO- PO_4^{3-}) (e); MBPO and defective hexagonal $BiPO_4$ (MBPO- PO_4^{3-}) (f).

could induce the formation of an intermediate level in the band gap for both samples. This mid level would lower the photo energy required for electron transition, which is beneficial for guiding the electrons hopping from valence band to conduction band through middle level efficiently.

3.3. Morphological structures

The scanning electron microscopy (SEM) show that the HBPO and Bi-HBPO-102 consist of large-scale sheet-shaped architecture stack assembled by thick nanosheets in Fig. 3a and b, separately. The Bi particles are attached on the surface of the Bi-HBPO-102 as shown in Fig. 3c and d. In the HRTEM image of Bi-HPBO-102 (Fig. 3e), the lattice spacing of d = 0.280 nm matches well with the {102} hexagonal phase of $BiPO_4$ (HBPO), which can be directly illustrated the exposed facet of {102} on Bi-HBPO-102. Meanwhile, a lattice spacing of 0.234 nm is corresponded to the Bi metal with {104} facet. TEM image of Bi-HBPO-102 further confirms the sheet-shaped structure in Fig. 3f.

For MBPO and Bi-MBPO-120, irregular sheet-shaped nanostructures can be observed in Fig. 4. Granule of Bi metals spread on the surface of Bi-MBPO-120 in Fig. 4c and d, which also suggest that the accumulated Bi particles on Bi-MBPO-120 is less than the Bi-HBPO-102. TEM image of Bi-MBPO-120 displays the nanosheets-like morphology in Fig. 4e. Furthermore, the HRTEM image in Fig. 4f, showing that the fringe space of 0.309 nm is corresponded to {120} monoclinic phase of $BiPO_4$ (MBPO) that verifies the exposed facet of Bi-MBPO-120. Similarly, the Bi metal particles is formed on the surface of MBPO with the lattice spaces of d = 0.157 nm assigned to the {107} facet of Bi metal from the Fig. 4f.

Fig. S2 shows the N_2 adsorption-desorption isotherms. Obviously, all the samples show the representative isotherms of type IV and hysteresis loop of type H3 at high relative pressure (P/P_0). The pore size

distribution ranges broadly from 1.0 to 250 nm (insert in Fig. S2). It is worth nothing that the surface areas of the four samples are increased in sequence of MBPO (4.6 m^2/g) < Bi-MBPO-120 (6.0 m^2/g) < HBPO (8.2 m^2/g) < Bi-HBPO-102 (10.6 m^2/g), which can be attributed to the granule of numerous Bi metal accumulated on the surface of the Bi-MBPO-120 and Bi-HBPO-102. The slightly increased surface areas are beneficial for NO adsorption and photocatalysis reaction on the photocatalysts.

3.4. Photocatalytic performance and charge transfer pathway

The photocatalytic performance of the as-prepared samples is evaluated by removal of NO in air under visible light irradiation. NO is stable without direct photolysis under visible light irradiation [41,42]. In Fig. 5a, the NO removal ratios for pure MBPO and HBPO are merely 2.0% due to their large band gap. Importantly, the deposition of Bi metal on Bi-MBPO-120 and Bi-HBPO-102 makes the NO removal ratios increase to 36.2 and 51.4% significantly. Remarkably, the Bi-HBPO-102 exhibits more efficient activity than Bi-MBPO-120. The highly enhanced visible light activity should be ascribed to the synergistic effects of phosphate defect and Bi metal. On one band, the phosphate defect modifies the band structure of $BiPO_4$ with different phases and make them visible light active (Fig. 2e and f). On the other hand, as can be observed from the SEM images (Figs. 3d and 4 d), the Bi particles are accumulated on the surface of Bi-MBPO-120 and Bi-HBPO-102. Due to the surface plasmon resonance effects, the Bi metal can act as a co catalyst for enhancing the charge separation and thus increasing the visible light photocatalytic activity. We have measured the action spectra of the optimized photocatalyst as shown in Fig. S3. The results showed that the photocatalytic activity is dependent on the wavelength of the visible light. The photocatalytic activity is increased as the energy of the light is increased.
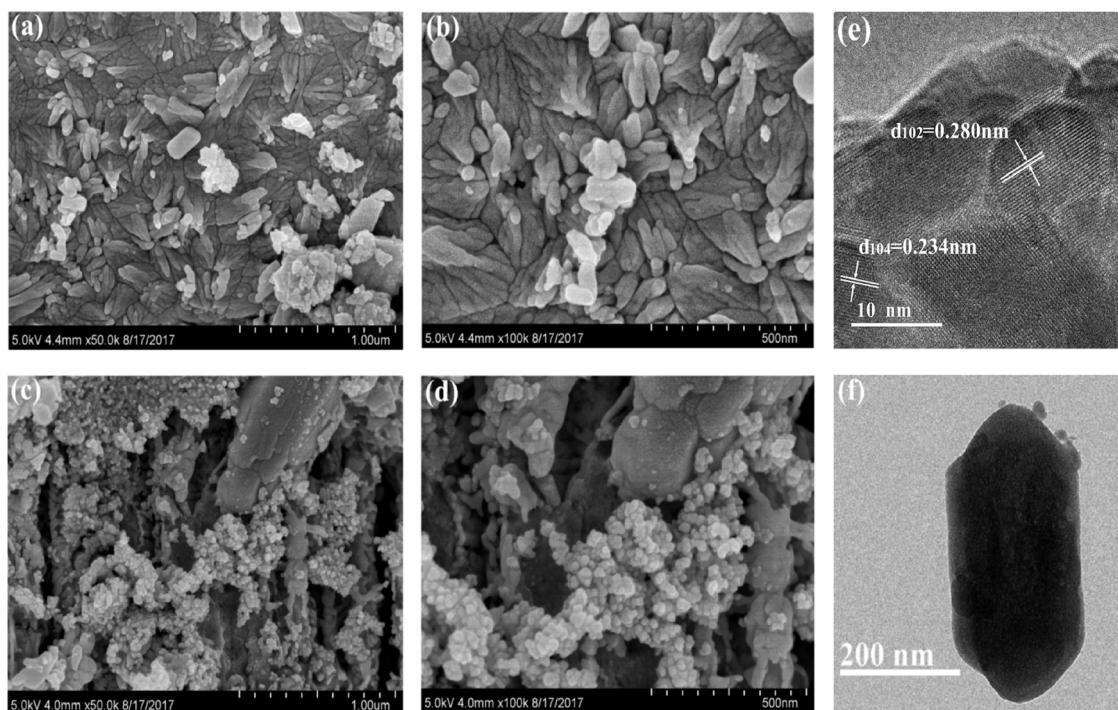
Fig. 3. SEM images of HBPO (a, b) and Bi-HBPO-102 (c, d); HRTEM and TEM images of Bi-HBPO-102 (e, f).

Fig. 5b shows the optical properties of the as-synthesized samples. All the samples exhibit an absorption edge at 280–370 nm in the UV light region. Notably, the absorption edges of Bi-HBPO-102 and Bi-MBPO-120 show slightly red-shifts in comparison with the HBPO and MBPO. Additionally, Bi-HBPO-102 and Bi-MBPO-120 wield entire visible light adsorption because of the SPR effect from Bi metal and the phosphate defect.

To clarify the generation, transfer, and recombination of the charge carriers pathway, the photoluminescence emission (PL) was carried out. In Fig. S4, the PL intensity of Bi-HBPO-102 and Bi-MBPO-120 are lower than that of the pure $BiPO_4$ (HBPO and MBPO) because the metal Bi could promote the separation efficiency of photogenerated charge carriers. Obviously, the peak intensity of Bi-HBPO-102 is much lower than Bi-MBPO-120, which implies that the Bi-HBPO-102 charge recombination has been largely inhibited. This is also consistent with the trend of the photocatalytic removal of NO under visible light irradiation (Fig. 5a), where the Bi-HBPO-102 performs better than Bi-MBPO-120 on NO removal.

To further explore how the Bi metal influence the charge separation and transfer processes on $BiPO_4$, the DFT is applied to calculate the
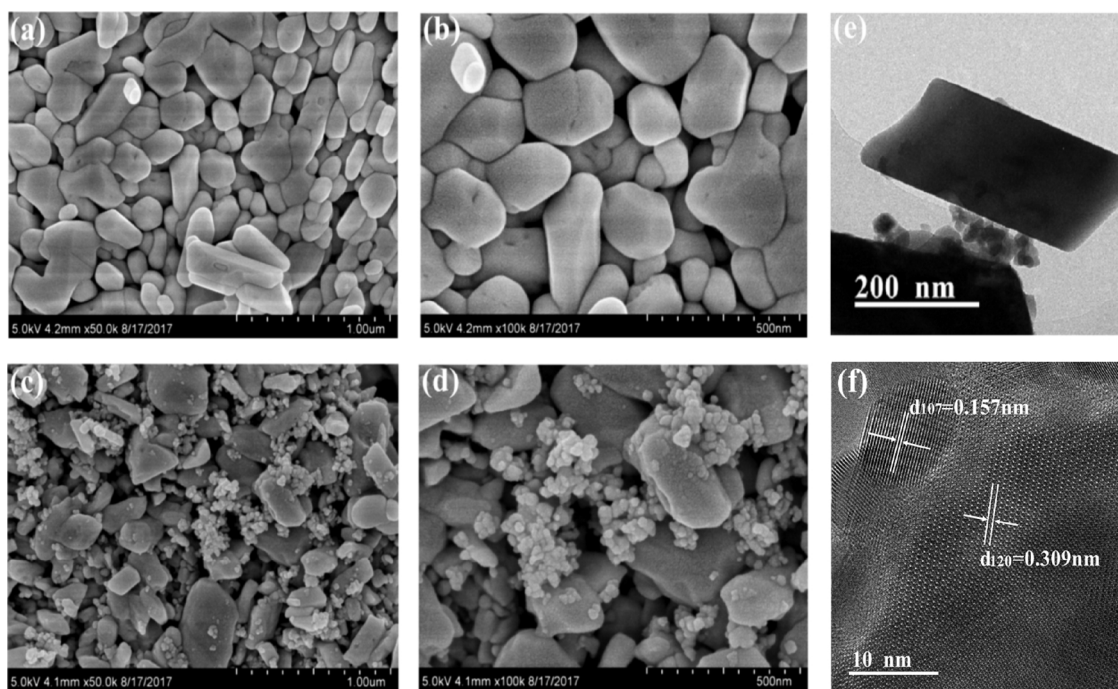

Fig. 4. SEM images of MBPO (a, b) and Bi-MBPO-120 (c, d); TEM and HRTEM images of Bi-MBPO-120 (e, f).
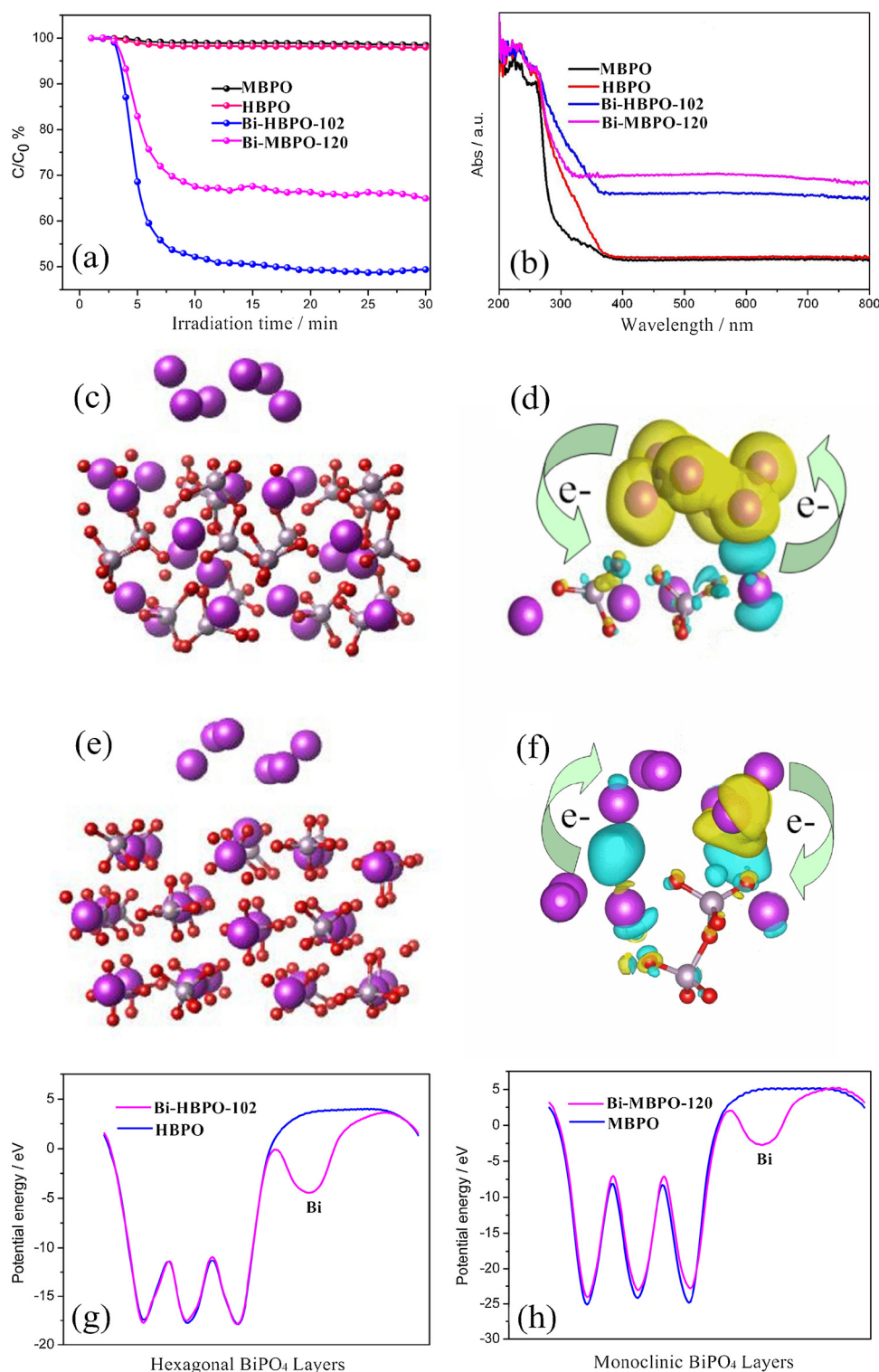
Fig. 5. Photocatalytic activity of MBPO, HBPO, Bi-HBPO-102 and Bi-MBPO-120 under visible light irradiation (a); UV–vis DRS spectra of MBPO, HBPO, Bi-HBPO-102, Bi-MBPO-102 (b); the side views of Bi-HBPO-102) and Bi-MBPO-120 (c, e); Charge difference distribution of Bi-HBPO-102) and Bi-MBPO-120, respectively. And the charge accumulation is in blue and depletion in yellow (d, f); electrostatic potential of Bi-HBPO-102 and Bi-MBPO-120 (g, h). (For interpretation of the references to colour in this figure legend, the reader is referred to the web version of this article).

charge difference distribution and electrostatic potential. Fig. 5c and e display the optimized electronic structure of Bi-HBPO-102 and Bi-MBPO-120, respectively. In Fig. 5d and f, a covalent loop is generated at the interface along the path of $[Bi_2O_2]^{2+}$ → Bi metal → PO_4^{3-} on Bi-HBPO-102 and Bi-MBPO-120. This result suggests that the electrons in the outer orbit of $[Bi_2O_2]^{2+}$ has a tendency to transfer to Bi metal. Then

the obtained electrons of Bi metal migrate to PO_4^{3-} along with the SPR hot electrons which contribute to electrons migration in a steered direction [17,24]. Fig. 5g and h show the electrostatic potential of all the samples. The peak bottom depicts the position of the bulk structure of BiPO_4 and the peak top illustrates the lowest energy barriers that must be overcome to initiate the excitation. Interestingly, the potential
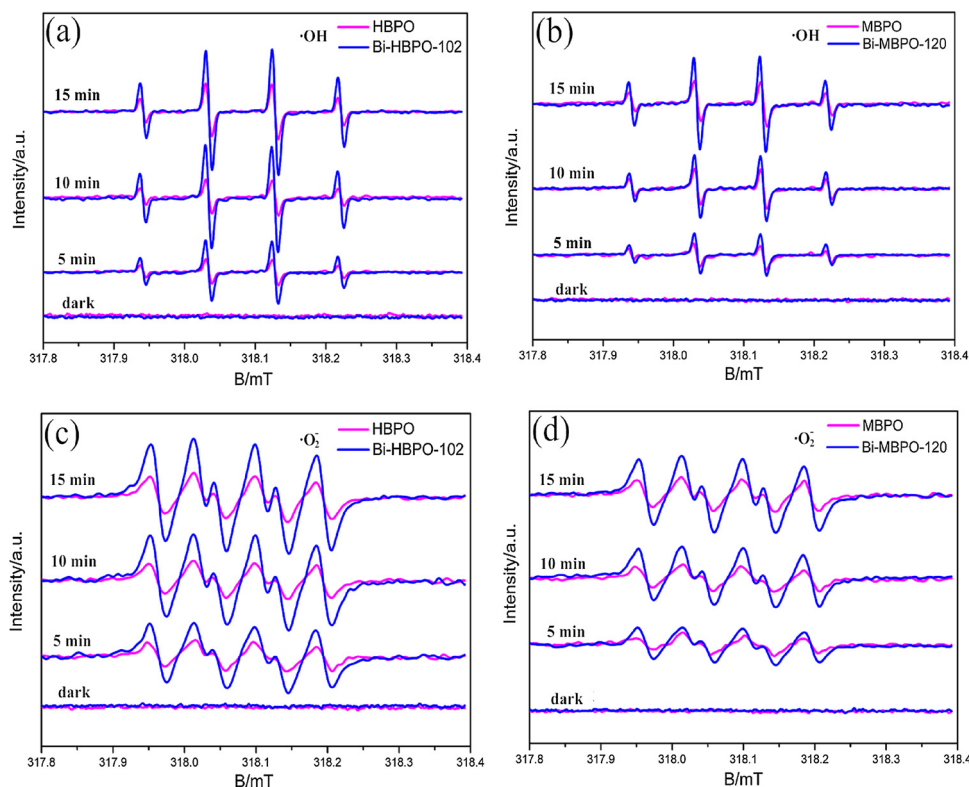
Fig. 6. DMPO ESP spectra in dark and under visible light (λ ≥ 420 nm) for 15 min, respectively in queous dispersion for ·OH (a, b) and methanol dispersion for ·O_2^- (c, d) of Bi-HBPO-102 and Bi-MBPO-120.

energy of Bi metal is revealed for both the samples, which benefits to the electrons transfer from Bi metal cross the barrier and thus enables the optimized interfacial electron transfer [43]. Additionally, Bi-HBPO-102 has a much lower potential barrier (-17.5 eV) than the Bi-MBPO-120 (-24.9 eV), which could further promote transport of charge carriers and increase adsorption and activation of the gas molecules.

3.5. Photocatalysis reaction mechanism for NO oxidation

In order to further demonstrate the roles of main reactive species in the photocatalytic NO oxidation, the DMPO spin-trapping ESR is applied in aqueous dispersion for ·OH radicals in Fig. 6a and b and in ethanol dispersion for ·O_2 radicals in Fig. 6c and d. On the one hand, with the illumination of visible light, the signal intensities of the ·OH radicals and the ·O_2 radicals are both enhanced for Bi-HBPO-102 and Bi-MBPO-120, respectively. The results illustrate that the two radicals act as the major active species in the reaction process. On the other hand, the signal intensities of ·OH and ·O_2 of Bi-HBPO-102 are apparently stronger than Bi-MBPO-120 because of the Bi-HBPO-102 with a lower potential energy barrier of -17.5 eV (Fig. 5g). This result indicates that the specific electronic structure of Bi-HBPO-102 could highly facilitate the charge separation and thus generate more active radicals for photocatalytic NO removal.

The in situ DRIFTS are employed to reveal the molecular photocatalytic reaction mechanism on Bi-HBPO-102 and Bi-MBPO-120 (Fig. 7). Table 1 and Table 2 present the assignment of the IR peaks observed during NO adsorption and oxidation over samples. The absorption peaks of NO (1037, 1350, and 1407 cm^{-1}), NO_2 (1443 cm^{-1}), N_2O_5 (860 cm^{-1}) have been detected on the surface of Bi-HBPO-102 (Fig. 7a) because of the physical adsorption of NO [44–46]. With the increasing of absorption time, the bands of the monodentate nitrates (1148 cm^{-1}) [47] and bidentate nitrite (1257 and 1481 cm^{-1}) [48,49] can be detected (Fig. 7a). For the Bi-MBPO-120 in Fig. 7b, typical peaks can be observed at 1066 cm^{-1} for NO [44], 950 cm^{-1} for NO_2 [45],

920 cm^{-1} for N_2O_4 [46], 1122 cm^{-1} [47] for monodentate nitrates, 1206 cm^{-1} and 1465 cm^{-1} [50,51] for bidentate nitrite. In general, during the absorption process, the surface active radicals will oxide the NO into more stable monodentate nitrite species on the Bi-HBPO-102 and Bi-MBPO-120. After absorption equilibrium reached, the band of NO (1066 cm^{-1} and 1413 cm^{-1}) [44] can be observed on Bi-HBPO-102 (Fig. 7c), and the NO band at 1072 cm^{-1} [44] is noted in Fig. 7d, which can be attributed to the chemical NO absorption on Bi-HBPO-102 and Bi-MBPO-120.

When the visible light irradiation, the ·O_2^- and ·OH can be generated on conduction band (Eq.1) and valence band (Eq. 2), respectively. With the increasing of the irradiation, it is worth to note that an obvious adsorption band of NO^+ at 2225 cm^{-1} [52] can be observed on Bi-HBPO-102 (Fig. 7c), which can be ascribed to the reaction intermediate product of NO oxidation. Additionally, the bands appear at 856 cm^{-1} for nitrate, 1482 cm^{-1} for bidentate nitrate, 1000 cm^{-1} and 1270 cm^{-1} for bridging nitrates [53,46,54]. Therefore, we propose that the absorbed NO can be oxidized via a new reaction pathway. A part of the NO could lose an electron probably to the phosphate defect and transform to NO^+ (Eq. 3), then the NO^+ can be subsequently oxidized by the ·OH to the nitrite species and nitrate species (Eqs. (4) and (5)) [49,55]. Overall, the above result implies that the phosphate defect could facilitate the activation of NO via the formation of NO^+ to promote the photo-oxidation of NO. In contrast with the ESR results (Fig. 6), the Bi-HBPO-102 could produce more active radicals than Bi-MBPO-120, which is favorable for the NO removal. Interestingly, as shown in Fig. 7c, the NO_2 peak located at the peak of 1441 cm^{-1} can be hardly detected on Bi-HBPO-102 [54]. On the contrary, the bands of NO_2 at 1220 cm^{-1} and 948 cm^{-1} [49] has been detected on Bi-MBPO-120 in Fig. 7d, which illustrates that the special electronic structure of Bi-HBPO-102 can inhibit the toxic product of NO_2.

For Bi-MBPO-120, the oxidation pathway of NO is different from the Bi-HBPO-102. At first, the NO was oxidized to NO_2 by O_2 (Eq. 6). Then, the NO_2 receives electrons from Bi metal due to the SPR effect and
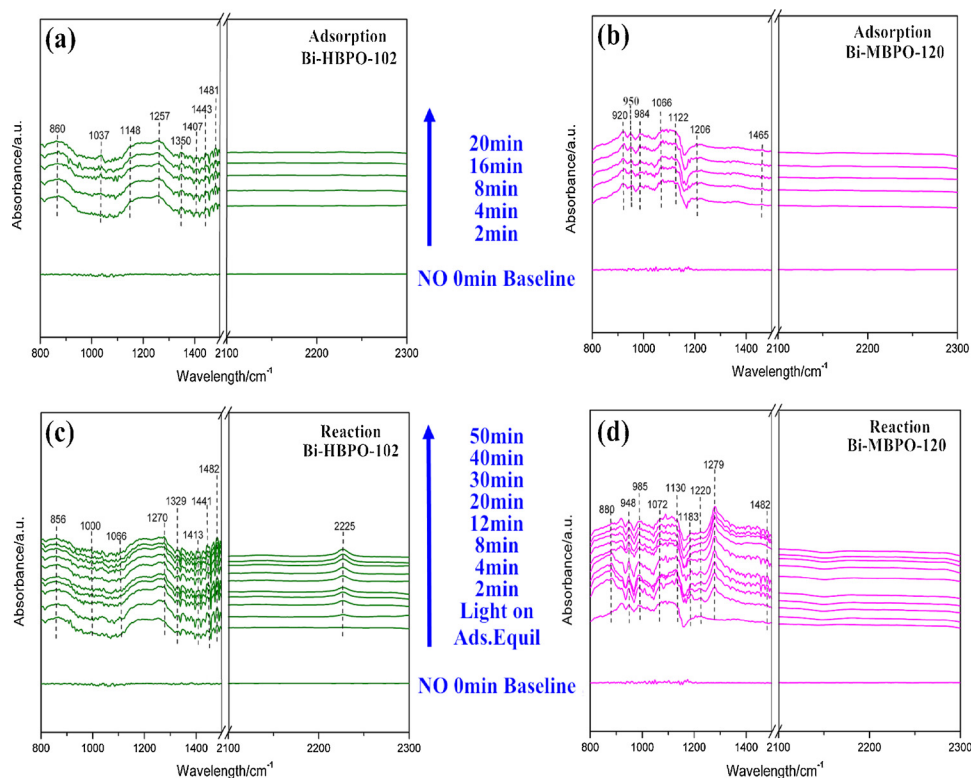
Fig. 7. In situ IR spectra of NO adsorption and photocatalytic reaction processes over Bi-HBPO-102 (a, c) and Bi-MBPO-120 (b, d).

Table 1
Assignments of the IR bands observed during the NO adsorption over Bi-HBPO-102 and Bi-MBPO-120.
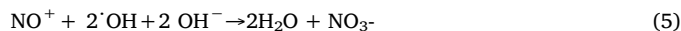
Wave number (cm^{-1})	Band assignment	References
1037, 1350, 1407, 1066	NO	[44]
1443, 950	NO_2	[45]
860	N_2O_5	[46]
1148, 1122	Monodentate nitrates	[47]
1257, 1481, 1206, 1465	Bidentate nitrite	[48,49,50,51]
920	N_2O_4	[46]
1000, 1270	Bridging nitrites	[48,49]

Table 2
Assignments of the IR bands observed during the NO oxidation over Bi-HBPO-102 and Bi-MBPO-120.

Wave number (cm^{-1})	Band assignment	References
1066, 1413, 1072	NO	[44]
1130	NO_3^-	[49]
856	NO_2^-	[53]
880	Bridging nitrite	[55]
1279, 1482	Bidentate nitrates	[57,58]
985, 1000, 1270	Bridging nitrates	[54]
2225	NO^+	[52]
948, 1220, 1441	NO_2	[49,54]

transform to more stable bridging nitrites (Eq. 7) assigned at 880 cm^{-1} [55] in Fig. 7d. After that, the h^+ and $\cdot O_2^-$ could oxidize the bridging nitrites to nitrates (Eq. 8). In Fig. 7d, the bands have already been noted at 985 cm^{-1} [54] (bridging nitrate), 1279 cm^{-1} [56,57] and 1482 cm^{-1} [58] (bidentate nitrate). Note the nitrate on the catalyst surface can be easily removal by water washing [59].

$$e^- + O_2 \rightarrow \cdot O_2^- \tag{1}$$

$$h^+ + OH^- \rightarrow \cdot OH \tag{2}$$

$$NO + \cdot OH \rightarrow NO^+ + OH^- \tag{3}$$

$$NO^+ + 2OH^- \rightarrow H_2O + NO_2\text{-} \tag{4}$$

$$NO^+ + 2\cdot OH + 2\ OH^- \rightarrow 2H_2O + NO_3\text{-} \tag{5}$$

$$NO + O_2 \rightarrow NO_2 \tag{6}$$

$$NO_2 + e^- \rightarrow NO_2\text{-} \tag{7}$$

$$2NO_2^- + \cdot O_2\text{-} + h^+ \rightarrow 2NO_3\text{-} \tag{8}$$

According to the experimental and theoretical results, the photocatalytic reaction processes on Bi-HBPO-102 and Bi-MBPO-120 consist of four steps. As shown in Fig. 8, accompanying by the formation of intermediate level of phosphate defects, the electrons on the valence band are excited to the defect level under visible light illumination (path 1). Then, some of electrons on defect level can be further hopped to the CB (path 2). In addition, another part of electrons from the defect level are transferred to the metal Bi (path 3). The Bi metals play the two functions that can transfer the electrons endowed by intermediate level and hot electrons formed by the SPR effect of metal Bi to the conduction band (path 4). This mechanism is also supported by Fig. 5d and f where a covalent loop is formed at the interface along the process of $[Bi_2O_2]^{2+} \rightarrow$ Bi metal $\rightarrow PO_4^{3-}$ on Bi-HBPO-102 and Bi-MBPO-120.

4. Conclusion

In summary, Bi metal deposited hexagonal@defective $BiPO_4$ with the exposure of {102} facet (Bi-HBPO-102) and Bi metal deposited monoclinic@defective $BiPO_4$ with the exposure of {120} facet (Bi-MBPO-120) were prepared by the chemical deposition method and a one-step solvothermal approach, respectively. The visible light photocatalytic NO removal performance of $BiPO_4$ was highly promoted because of the synergistic effects of Bi metals and phosphate defects. The Bi metal acted as both the electron contributor and electron conductor, which could promote the charge carriers separation efficiency. With the introduction of phosphate defects and the formation of the intermediate
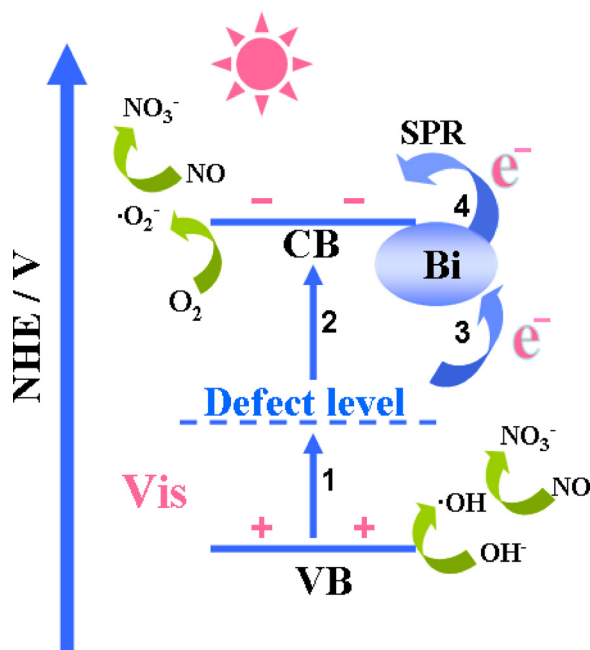
Fig. 8. The proposed photocatalysis mechanism on Bi-HBPO-102 and Bi-MBPO-120.

level was realized, constructing a new charge transfer pathway of a covalent loop at the interface along the path of $[Bi_2O_2]^{2+} \rightarrow$ Bi metal $\rightarrow PO_4^{3-}$ on the Bi-HBPO-102 and Bi-MBPO-120. The Bi-HBPO-102 exhibited higher photocatalytic activity than the Bi-MBPO-120. The {102} facet with the stronger distorted PO_4^{3-} tetrahedron and the lower potential energy barrier (-17.5 eV) contributed to the contacted interface with the more efficient charge transfer, and thus promoted the generation of active radicals on {102} facet. Moreover, we observed the peak of NO^+ on Bi-HBPO-102 during using the in situ DRIFTS during the reaction process of photocatalytic oxidation NO. The formation of NO^+ is beneficial for the NO oxidation. The new charge transfer pathway and photocatalysis mechanism were proposed. The present work could provide new insight into the development of defects-containing photocatalysts and gas-phase photocatalytic reaction mechanism.

References

[1] A.L. Linsebigler, G. Lu, J.T. Yates Jr, Chem. Rev. 95 (1995) 735–758.
[2] Z. Shayegan, C.S. Lee, F. Haghighat, Chem. Eng. J. 334 (2018) 2408–2439.
[3] A. Fujishima, K. Honda, Nature 238 (1972) 238–245.
[4] J.C.S. W, Y.T. Cheng, J. Catal. 237 (2006) 393-404.
[5] Z. Zeng, P. Lu, C. Li, L. Mai, Z. Li, Y. Zhang, Catal. Sci. Technol. 11 (2012) 2188–2199.
[6] W. Cui, J. Li, W. Cen, Y. Sun, S. Lee, F. Dong, J. Catal. 352 (2017) 351–360.
[7] Y. Sun, X. Xiao, X. Dong, F. Dong, W. Zhang, Chin. J. Catal. 38 (2017) 217–226.
[8] A. Luz, C. Feldmann, Solid State Sci. 13 (2011) 1017–1021.
[9] X. Zhang, Z. Ai, F. Jia, L. Zhang, J. Phys. Chem. C 112 (2008) 747–753.
[10] M. Long, P. Hu, H. Wu, J. Cai, B. Tan, B. Zhou, Appl. Catal. B Environ. 184 (2016) 20–27.
[11] X. Li, W. Zhang, J. Li, G. Jiang, Y. Zhou, S. Lee, F. Dong, Appl. Catal. B Environ. 241 (2019) 187–195.
[12] M. Ge, Y. Li, L. Liu, Z. Zhou, W. Chen, J. Phys. Chem. C 115 (2011) 5220–5225.
[13] X. Liu, H. Cao, J. Yin, Nano Res. 4 (2011) 470–482.
[14] P. Madhusudan, J. Ran, J. Zhang, J. Yu, G. Liu, Appl. Catal. B Environ. 110 (2011) 286–295.
[15] J. Yu, A. Kudo, Adv. Funct. Mater. 16 (2006) 2163–2169.
[16] Y. He, L. Zhang, B. Teng, M. Fan, Environ. Sci. Technol. 49 (2014) 649–656.
[17] Z. Jiang, X. Liang, H. Zheng, Y. Liu, X. Zhang, P. Wang, X. Zhang, X. Qin, Y. Dai, M.H. Whangbo, B. Huang, Appl. Catal. B Environ. 219 (2017) 209–215.
[18] Z. Zhang, W. Wang, S. Meng, W. Yin, J. Hazard. Mater. 177 (2010) 1013–1018.
[19] B. Kiskan, J. Zhang, X. Wang, M. Antonietti, Y. Yagci, ACS Macro Lett. 1 (2012) 546–549.
[20] Y. Zhu, Q. Ling, Y. Liu, Wang H, Y. Zhu, Appl. Catal. B Environ. 187 (2016) 204–211.
[21] D. Liu, W. Cai, Y. Wang, Y. Zhu, Appl. Catal. B Environ. 236 (2018) 205–211.
[22] Y. Lv, Y. Zhu, Y. Zhu, J. Phys. Chem. C 117 (2013) 18520–18528.
[23] Y. Liu, Y. Lv, Y. Zhu, D. Liu, R. Zong, Y. Zhu, Appl. Catal. B Environ. 147 (2014) 851–857.
[24] J. Li, X. Dong, Y. Sun, W. Cen, F. Dong, Appl. Catal. B Environ. 226 (2018) 269–277.
[25] H. Wang, X. Yuan, Y. Wu, G. Zeng, W. Tu, C. Sheng, Y. Deng, F. Chen, J. Chew, Appl. Catal. B Environ. 209 (2017) 543–553.
[26] W. Fang, Z. Jiang, L. Yu, H. Liu, W. Shangguan, C. Terashima, A. Fujishima, J. Catal. 352 (2017) 155–159.
[27] G. Jiang, X. Li, M. Lan, T. Shen, X. Lv, F. Dong, S. Zhang, Appl. Catal. B Environ. 205 (2017) 532–540.
[28] Y. Cao, P. Maitarad, M. Gao, T. Taketsugu, H. Li, L. Shi, D. Zhang, Appl. Catal. B Environ. 238 (2018) 51–60.
[29] M. Lu, J. Fang, L. Han, K. Faungnawakij, H. Li, S. Cai, L. Shi, H. Jiang, D. Zhang, Nanoscale 10 (2018) 10528–10537.
[30] J. Zhao, Z. Chen, J. Am. Chem. Soc. 139 (2017) 12480–12487.
[31] G. Kresse, J. Furthmüller, Phys. Rev. B 54 (1996) 11169–11186.
[32] G. Kresse, J. Furthmüller, Comp. Mater. Sci. 6 (1996) 15–50.
[33] J. Perdew, K. Burke, M. Ernzerhof, Phys. Rev. Lett. 77 (1996) 3865–3868.
[34] P.E. Blöchl, Phys. Rev. B 50 (1994) 17953–17979.
[35] G. Kresse, D. Phys. Rev. B 59 (1999) 1758–1775.
[36] J. Heyd, G.E. Scuseria, M. Ernzerhof, J. Chem. Phys. 118 (2003) 8207–8215.
[37] J. Heyd, G.E. Scuseria, M. Ernzerhof, J. Chem. Phys. 124 (2006) 219906.
[38] D. Lide, CRC Handbook of Chemistry and Physics, 84th, CRC Press, 2003.
[39] Z. Wang, S. Yan, Y. Sun, T. Xiong, F. Dong, W. Zhang, Appl. Catal. B Environ. 214 (2017) 148–157.
[40] Z. Zhao, W. Zhang, X. Lv, Y. Sun, F. Dong, Y. Zhang, Environ. Sci. Nano 3 (2016) 1306–1317.
[41] I. Nakamura, N. Negishi, S. Kutsuna, T. Ihara, S. Sugihara, K. Takeuchi, J. Mol. Catal. A Chem. 161 (2000) 205–212.
[42] T. Xia, Y. Zhang, J. Murowchick, X. Chen, Catal. Today 225 (2014) 2–9.
[43] X. Dong, W. Zhang, Y. Sun, J. Li, W. Cen, Z. Cui, H. Huang, F. Dong, J. Catal. 357 (2018) 41–50.
[44] K. Hadjiivanov, H. Knozinger, Phys. Chem. Chem. Phys. 2 (2000) 2803–2806.
[45] B. Tsyntsarski, V. Avreyska, H. Kolev, T. Marinova, D. Klissurski, K. Hadjiivanov, J. Mol. Catal. A Chem. 193 (2003) 139–149.
[46] J.C.S. Wu, Y.T. Cheng, J. Phys. Chem. C 237 (2006) 394–404.
[47] M. Kantcheva, J. Catal. 204 (2001) 479–494.
[48] S.J. Huang, A.B. Walters, M.A. Vannice, J. Catal. 192 (2000) 29–47.
[49] N. Tang, Y. Liu, H. Wang, Z. Wu, J. Phys. Chem. C 115 (2011) 8214–8220.
[50] M. Kantcheva, A.S. Vakkasoglu, J. Catal. 223 (2004) 352–363.
[51] Z. Liu, J. Li, J. Hao, Chem. Eng. J. 165 (2010) 420–425.
[52] K. Hadjiivanov, V. Avreyska, D. Klissurski, T. Marinova, Langmuir 18 (2012) 1619–1625.
[53] G. Ramis, G. Busca, V. Lorenzelli, P. Forzatti, Appl. Catal. 64 (1990) 243–257.
[54] M. Iwamoto, H. Yahiro, N. Mizuno, W. Zhang, Y. Mine, H. Furukawa, S. Kagawa, J. Phys. Chem. 96 (1992) 9360–9366.
[55] L. Zhong, Y. Yu, W. Cai, X. Geng, Q. Zhong, Phys. Chem. Chem. Phys. 17 (2015) 15036–15045.
[56] Y. Zhou, Z. Zhao, F. Wang, K. Cao, D.E. Doronkin, F. Dong, J.D. Grunwaldt, J. Hazard. Mater. 307 (2016) 163–172.
[57] T. Weingand, S. Kuba, K. Hadjiivanov, H. Knzinger, J. Catal. 209 (2002) 539–546.
[58] W. He, Y. Sun, G. Jiang, Y. Li, X. Zhang, Y. Zhang, Y. Zhou, F. Dong, Appl. Catal. B Environ. 239 (2018) 619–627.
[59] P. Chen, H. Wang, H. Liu, Z. Ni, J. Li, Y. Zhou, F. Dong, Appl. Catal. B Environ. 242 (2019) 19–30.